Title
Searches for neutrinos from cosmic-ray interactions in the Sun using seven years of IceCube data

Journal
Journal of Cosmology and Astroparticle Physics, 2021(2)

ISSN
1475-7516

Authors
Aartsen, MG
Ackermann, M
Adams, J
et al.

Publication Date
2021-02-01

DOI
10.1088/1475-7516/2021/02/025

Peer reviewed

Prepared for submission to JCAP

Searches for neutrinos from cosmic-ray interactions in the Sun using seven years of IceCube data

M. G. Aartsen,[15] M. Ackermann,[54] J. Adams,[15] J. A. Aguilar,[11] M. Ahlers,[19] M. Ahrens,[45] C. Alispach,[25] K. Andeen,[36] T. Anderson,[51] I. Ansseau,[11] G. Anton,[23] C. Argüelles,[13] J. Auffenberg,[0] S. Axani,[13] P. Backes,[0] H. Bagherpour,[15] X. Bai,[42] A. Balagopal V.,[28] A. Barbano,[25] S. W. Barwick,[27] B. Bastian,[54] V. Baum,[35] S. Baur,[11] R. Bay,[7] J. J. Beatty,[17,18] K.-H. Becker,[53] J. Becker Tjus,[10] S. BenZvi,[44] D. Berley,[16] E. Bernardini,[54,a] D. Z. Besson,[29,b] G. Binder,[7,8] D. Bindig,[53] E. Blaufuss,[16] S. Blot,[54] C. Bohm,[45] S. Böser,[35] O. Botner,[52] J. Böttcher,[0] E. Bourbeau,[19] J. Bourbeau,[34] F. Bradascio,[54] J. Braun,[34] S. Bron,[25] J. Brostean-Kaiser,[54] A. Burgman,[52] J. Buscher,[0] R. S. Busse,[37] T. Carver,[25] C. Chen,[5] E. Cheung,[16] D. Chirkin,[34] S. Choi,[47] K. Clark,[30] L. Classen,[37] A. Coleman,[38] G. H. Collin,[13] J. M. Conrad,[13] P. Coppin,[12] P. Correa,[12] D. F. Cowen,[50,51] R. Cross,[44] P. Dave,[5] C. De Clercq,[12] J. J. DeLaunay,[51] H. Dembinski,[38] K. Deoskar,[45] S. De Ridder,[26] P. Desiati,[34] K. D. de Vries,[12] G. de Wasseige,[12] M. de With,[9] T. DeYoung,[21] A. Diaz,[13] J. C. Díaz-Vélez,[34] H. Dujmovic,[28] M. Dunkman,[51] E. Dvorak,[42] B. Eberhardt,[34] T. Ehrhardt,[35] P. Eller,[51] R. Engel,[28] P. A. Evenson,[38] S. Fahey,[34] A. R. Fazely,[6] J. Felde,[16] K. Filimonov,[7] C. Finley,[45] D. Fox,[50] A. Franckowiak,[54] E. Friedman,[16] A. Fritz,[35] T. K. Gaisser,[38] J. Gallagher,[33] E. Ganster,[0] S. Garrappa,[54] L. Gerhardt,[8] K. Ghorbani,[34] T. Glauch,[24] T. Glüsenkamp,[23] A. Goldschmidt,[8] J. G. Gonzalez,[38] D. Grant,[21] T. Grégoire,[51] Z. Griffith,[34] S. Griswold,[44] M. Günder,[0] M. Gündüz,[10] C. Haack,[0] A. Hallgren,[52] R. Halliday,[21] L. Halve,[0] F. Halzen,[34] K. Hanson,[34] A. Haungs,[28] D. Hebecker,[9] D. Heereman,[11] P. Heix,[0] K. Helbing,[53] R. Hellauer,[16] F. Henningsen,[24] S. Hickford,[53] J. Hignight,[22] G. C.

Hill,[1] K. D. Hoffman,[16] R. Hoffmann,[53] T. Hoinka,[20] B. Hokanson-Fasig,[34] K. Hoshina,[34,c] F. Huang,[51] M. Huber,[24] T. Huber,[28,54] K. Hultqvist,[45] M. Hünnefeld,[20] R. Hussain,[34] S. In,[47] N. Iovine,[11] A. Ishihara,[14] G. S. Japaridze,[4] M. Jeong,[47] K. Jero,[34] B. J. P. Jones,[3] F. Jonske,[0] R. Joppe,[0] D. Kang,[28] W. Kang,[47] A. Kappes,[37] D. Kappesser,[35] T. Karg,[54] M. Karl,[24] A. Karle,[34] U. Katz,[23] M. Kauer,[34] J. L. Kelley,[34] A. Kheirandish,[34] J. Kim,[47] T. Kintscher,[54] J. Kiryluk,[46] T. Kittler,[23] S. R. Klein,[7,8] R. Koirala,[38] H. Kolanoski,[9] L. Köpke,[35] C. Kopper,[21] S. Kopper,[49] D. J. Koskinen,[19] M. Kowalski,[9,54] K. Krings,[24] G. Krückl,[35] N. Kulacz,[22] N. Kurahashi,[41] A. Kyriacou,[1] J. L. Lanfranchi,[51] M. J. Larson,[16] F. Lauber,[53] J. P. Lazar,[34] K. Leonard,[34] A. Leszczyńska,[28] M. Leuermann,[0] Q. R. Liu,[34] E. Lohfink,[35] C. J. Lozano Mariscal,[37] L. Lu,[14] F. Lucarelli,[25] J. Lünemann,[12] W. Luszczak,[34] Y. Lyu,[7,8] W. Y. Ma,[54] J. Madsen,[43] G. Maggi,[12] K. B. M. Mahn,[21] Y. Makino,[14] P. Mallik,[0] K. Mallot,[34] S. Mancina,[34] I. C. Mariş,[11] R. Maruyama,[39] K. Mase,[14] R. Maunu,[16] F. McNally,[32] K. Meagher,[34] M. Medici,[19] A. Medina,[18] M. Meier,[20] S. Meighen-Berger,[24] G. Merino,[34] T. Meures,[11] J. Micallef,[21] D. Mockler,[11] G. Momenté,[35] T. Montaruli,[25] R. W. Moore,[22] R. Morse,[34] M. Moulai,[13] P. Muth,[0] R. Nagai,[14] U. Naumann,[53] G. Neer,[21] H. Niederhausen,[24] M. U. Nisa,[21] S. C. Nowicki,[21] D. R. Nygren,[8] A. Obertacke Pollmann,[53] M. Oehler,[28] A. Olivas,[16] A. O'Murchadha,[11] E. O'Sullivan,[45] T. Palczewski,[7,8] H. Pandya,[38] D. V. Pankova,[51] N. Park,[34] P. Peiffer,[35] C. Pérez de los Heros,[52] S. Philippen,[0] D. Pieloth,[20] E. Pinat,[11] A. Pizzuto,[34] M. Plum,[36] A. Porcelli,[26] P. B. Price,[7] G. T. Przybylski,[8] C. Raab,[11] A. Raissi,[15] M. Rameez,[19] L. Rauch,[54] K. Rawlins,[2] I. C. Rea,[24] R. Reimann,[0] B. Relethford,[41] M. Renschler,[28] G. Renzi,[11] E. Resconi,[24] W. Rhode,[20] M. Richman,[41] S. Robertson,[8] M. Rongen,[0] C. Rott,[47] T. Ruhe,[20] D. Ryckbosch,[26] D. Rysewyk,[21] I. Safa,[34] S. E. Sanchez Herrera,[21] A. Sandrock,[20] J. Sandroos,[35] M. Santander,[49] S. Sarkar,[40] S. Sarkar,[22] K. Satalecka,[54] M. Schaufel,[0] H. Schieler,[28] P. Schlunder,[20] T. Schmidt,[16] A. Schneider,[34] J. Schneider,[23] F. G. Schröder,[28,38] L. Schumacher,[0] S. Sclafani,[41] D. Seckel,[38] S. Seunarine,[43] S. Shefali,[0] M. Silva,[34] R. Snihur,[34] J. Soedingrekso,[20] D. Soldin,[38] M. Song,[16] G. M. Spiczak,[43] C. Spiering,[54] J. Stachurska,[54] M. Stamatikos,[18] T.

Stanev,[38] R. Stein,[54] J. Stettner,[0] A. Steuer,[35] T. Stezelberger,[8] R. G. Stokstad,[8] A. Stößl,[14] N. L. Strotjohann,[54] T. Stürwald,[0] T. Stuttard,[19] G. W. Sullivan,[16] I. Taboada,[5] F. Tenholt,[10] S. Ter-Antonyan,[6] A. Terliuk,[54] S. Tilav,[38] K. Tollefson,[21] L. Tomankova,[10] C. Tönnis,[48] S. Toscano,[11] D. Tosi,[34] A. Trettin,[54] M. Tselengidou,[23] C. F. Tung,[5] A. Turcati,[24] R. Turcotte,[28] C. F. Turley,[51] B. Ty,[34] E. Unger,[52] M. A. Unland Elorrieta,[37] M. Usner,[54] J. Vandenbroucke,[34] W. Van Driessche,[26] D. van Eijk,[34] N. van Eijndhoven,[12] J. van Santen,[54] S. Verpoest,[26] M. Vraeghe,[26] C. Walck,[45] A. Wallace,[1] M. Wallraff,[0] N. Wandkowsky,[34] T. B. Watson,[3] C. Weaver,[22] A. Weindl,[28] M. J. Weiss,[51] J. Weldert,[35] C. Wendt,[34] J. Werthebach,[34] B. J. Whelan,[1] N. Whitehorn,[31] K. Wiebe,[35] C. H. Wiebusch,[0] L. Wille,[34] D. R. Williams,[49] L. Wills,[41] M. Wolf,[24] J. Wood,[34] T. R. Wood,[22] K. Woschnagg,[7] G. Wrede,[23] D. L. Xu,[34] X. W. Xu,[6] Y. Xu,[46] J. P. Yanez,[22] G. Yodh,[27] S. Yoshida,[14] T. Yuan[34] and M. Zöcklein[0]

[0]III. Physikalisches Institut, RWTH Aachen University, D-52056 Aachen, Germany

[1]Department of Physics, University of Adelaide, Adelaide, 5005, Australia

[2]Dept. of Physics and Astronomy, University of Alaska Anchorage, 3211 Providence Dr., Anchorage, AK 99508, USA

[3]Dept. of Physics, University of Texas at Arlington, 502 Yates St., Science Hall Rm 108, Box 19059, Arlington, TX 76019, USA

[4]CTSPS, Clark-Atlanta University, Atlanta, GA 30314, USA

[5]School of Physics and Center for Relativistic Astrophysics, Georgia Institute of Technology, Atlanta, GA 30332, USA

[6]Dept. of Physics, Southern University, Baton Rouge, LA 70813, USA

[7]Dept. of Physics, University of California, Berkeley, CA 94720, USA

[8]Lawrence Berkeley National Laboratory, Berkeley, CA 94720, USA

[9]Institut für Physik, Humboldt-Universität zu Berlin, D-12489 Berlin, Germany

[10]Fakultät für Physik & Astronomie, Ruhr-Universität Bochum, D-44780 Bochum, Germany

[11]Université Libre de Bruxelles, Science Faculty CP230, B-1050 Brussels, Belgium

[12]Vrije Universiteit Brussel (VUB), Dienst ELEM, B-1050 Brussels, Belgium

[13]Dept. of Physics, Massachusetts Institute of Technology, Cambridge, MA 02139, USA

[14]Dept. of Physics and Institute for Global Prominent Research, Chiba University, Chiba 263-8522, Japan

[15]Dept. of Physics and Astronomy, University of Canterbury, Private Bag 4800, Christchurch, New Zealand

[16]Dept. of Physics, University of Maryland, College Park, MD 20742, USA

[17]Dept. of Astronomy, Ohio State University, Columbus, OH 43210, USA

[18]Dept. of Physics and Center for Cosmology and Astro-Particle Physics, Ohio State University, Columbus, OH 43210, USA

[19]Niels Bohr Institute, University of Copenhagen, DK-2100 Copenhagen, Denmark
[20]Dept. of Physics, TU Dortmund University, D-44221 Dortmund, Germany
[21]Dept. of Physics and Astronomy, Michigan State University, East Lansing, MI 48824, USA
[22]Dept. of Physics, University of Alberta, Edmonton, Alberta, Canada T6G 2E1
[23]Erlangen Centre for Astroparticle Physics, Friedrich-Alexander-Universität Erlangen-Nürnberg, D-91058 Erlangen, Germany
[24]Physik-department, Technische Universität München, D-85748 Garching, Germany
[25]Département de physique nucléaire et corpusculaire, Université de Genève, CH-1211 Genève, Switzerland
[26]Dept. of Physics and Astronomy, University of Gent, B-9000 Gent, Belgium
[27]Dept. of Physics and Astronomy, University of California, Irvine, CA 92697, USA
[28]Karlsruhe Institute of Technology, Institut für Kernphysik, D-76021 Karlsruhe, Germany
[29]Dept. of Physics and Astronomy, University of Kansas, Lawrence, KS 66045, USA
[30]SNOLAB, 1039 Regional Road 24, Creighton Mine 9, Lively, ON, Canada P3Y 1N2
[31]Department of Physics and Astronomy, UCLA, Los Angeles, CA 90095, USA
[32]Department of Physics, Mercer University, Macon, GA 31207-0001, USA
[33]Dept. of Astronomy, University of Wisconsin, Madison, WI 53706, USA
[34]Dept. of Physics and Wisconsin IceCube Particle Astrophysics Center, University of Wisconsin, Madison, WI 53706, USA
[35]Institute of Physics, University of Mainz, Staudinger Weg 7, D-55099 Mainz, Germany
[36]Department of Physics, Marquette University, Milwaukee, WI, 53201, USA
[37]Institut für Kernphysik, Westfälische Wilhelms-Universität Münster, D-48149 Münster, Germany
[38]Bartol Research Institute and Dept. of Physics and Astronomy, University of Delaware, Newark, DE 19716, USA
[39]Dept. of Physics, Yale University, New Haven, CT 06520, USA
[40]Dept. of Physics, University of Oxford, Parks Road, Oxford OX1 3PU, UK
[41]Dept. of Physics, Drexel University, 3141 Chestnut Street, Philadelphia, PA 19104, USA
[42]Physics Department, South Dakota School of Mines and Technology, Rapid City, SD 57701, USA
[43]Dept. of Physics, University of Wisconsin, River Falls, WI 54022, USA
[44]Dept. of Physics and Astronomy, University of Rochester, Rochester, NY 14627, USA
[45]Oskar Klein Centre and Dept. of Physics, Stockholm University, SE-10691 Stockholm, Sweden
[46]Dept. of Physics and Astronomy, Stony Brook University, Stony Brook, NY 11794-3800, USA
[47]Dept. of Physics, Sungkyunkwan University, Suwon 16419, Korea
[48]Institute of Basic Science, Sungkyunkwan University, Suwon 16419, Korea
[49]Dept. of Physics and Astronomy, University of Alabama, Tuscaloosa, AL 35487, USA
[50]Dept. of Astronomy and Astrophysics, Pennsylvania State University, University Park, PA 16802, USA
[51]Dept. of Physics, Pennsylvania State University, University Park, PA 16802, USA
[52]Dept. of Physics and Astronomy, Uppsala University, Box 516, S-75120 Uppsala, Sweden
[53]Dept. of Physics, University of Wuppertal, D-42119 Wuppertal, Germany

[54]DESY, D-15738 Zeuthen, Germany
[a]also at Università di Padova, I-35131 Padova, Italy
[b]also at National Research Nuclear University, Moscow Engineering Physics Institute (MEPhI), Moscow 115409, Russia
[c]Earthquake Research Institute, University of Tokyo, Bunkyo, Tokyo 113-0032, Japan

E-mail: analysis@icecube.wisc.edu

Abstract. Cosmic-ray interactions with the solar atmosphere are expected to produce particle showers which in turn produce neutrinos from weak decays of mesons. These solar atmospheric neutrinos (SAνs) have never been observed experimentally. A detection would be an important step in understanding cosmic-ray propagation in the inner solar system and the dynamics of solar magnetic fields. SAνs also represent an irreducible background to solar dark matter searches and a detection would allow precise characterization of this background. Here, we present the first experimental search based on seven years of data collected from May 2010 to May 2017 in the austral winter with the IceCube Neutrino Observatory. An unbinned likelihood analysis is performed for events reconstructed within 5 degrees of the center of the Sun. No evidence for a SAν flux is observed. After inclusion of systematic uncertainties, we set a 90% upper limit of $1.02^{+0.20}_{-0.18} \cdot 10^{-13}$ GeV^{-1}cm^{-2}s^{-1} at 1 TeV.

Contents

1 Introduction

Neutrinos can be produced as a result of cosmic-ray interactions in the solar atmosphere. Cosmic rays interact with nuclei in the solar atmosphere, producing particle showers including pions and kaons. The decays of these mesons produce so called "Solar Atmospheric Neutrinos" (SAνs). Theoretical flux predictions of SAνs and detailed process discussions have been given in [1–8]. The neutrino production process in the solar atmosphere is similar to that of the terrestrial atmospheric neutrinos, with the notable difference that mesons generated in the solar atmosphere tend to decay before they can re-interact or lose a significant fraction of their energy, due to the larger and thinner atmosphere. As a result, the neutrino spectrum from the solar atmosphere is expected to be harder compared to that from the Earth, where the spectrum is steepened due to interactions of the secondary mesons, see *e.g.* [9]. This difference makes the spectra distinguishable and is used as a main criteria in our search for the SAν flux. A search for solar atmospheric neutrinos has never been experimentally performed and this work is the first of its kind.

The production process of SAνs is closely connected to that of gamma-rays through the decays of neutral pions and other mesons. Evidence for solar gamma rays was first reported in a re-analysis of EGRET data [10]. Recently, the Fermi-LAT Collaboration reported the observation of a steady gamma-ray emission from the solar disk with energies up to 10 GeV [11].

In addition to the solar disk emission predominantly due to neutral pion decays from cosmic-ray interactions in the solar atmosphere, an extended inverse Compton signal from cosmic-ray electron interactions with the solar photon field was also observed. A follow-up analysis on the solar disk emission based on six years of public Fermi-LAT data has shown that the energy spectrum extends beyond 100 GeV and anticorrelates with the solar activity [12]. This was confirmed with an extended nine year analysis [13]. The magnetic field near the Sun is complex and strongly time-dependent. Gamma-ray production is expected to be significantly enhanced above 10 GeV in case of a more intense magnetic field. However, the effects on the neutrino production are found to be negligible [14]. Further, the observed gamma-ray spectrum shows a potential dip [15] and points to an inhomogeneous emission between the equatorial plane and the polar region of the Sun [13]. Unexpectedly, the observed gamma-ray flux is about six times higher [12, 13] than theoretical predictions [1]. The High Altitude Water Cherenkov (HAWC) gamma-ray observatory has searched for gamma rays beyond the energies accessible by Fermi-LAT. HAWC reported no evidence of TeV gamma-ray emission in three years data and has set flux bounds [16]. The recent observation of gamma-ray emission from the Sun makes the search for solar atmospheric neutrinos very timely. The combined gamma-ray and neutrino data are expected to be vital to understand the solar atmospheric processes and cosmic-ray transport in the inner solar system [1, 17].

IceCube is the world's largest neutrino telescope and is optimized to detect high-energy (TeV) neutrinos. IceCube's acceptance to high-energy neutrinos and sub-degree-scale angular resolution to muon neutrinos makes it ideally suited to search for SAνs at TeV scales where the flux of SAνs is expected to dominate over that from terrestrial atmospheric neutrino backgrounds. In our analysis we rely on well established event selection criteria [18, 19] and a data set that has previously been used to study distant neutrino sources [18, 20, 21].

This paper is structured as follows: Section 2 describes the IceCube detector. Predictions for signal energy spectra and backgrounds to this analysis are given in Section 3. The data samples and the simulations are described in Section 4. Analysis method to search for SAνs and systematic uncertainties are given in Section 5. The results are presented in Section 6. Finally, Section 7 presents our conclusions and we discuss the prospects for future analysis and its applications.

2 The IceCube Neutrino Observatory

The IceCube Neutrino Observatory consists of the IceTop surface array [22] and the in-ice array [23] to detect Cherenkov light from relativistic charged particles, *e.g.* muons and electrons produced by high-energy neutrino interactions. The in-ice array is installed in the Antarctic ice at depths between 1450 m to 2450 m with 5160 Digital Optical Modules (DOMs) [23]. The in-ice array is comprised of 86 vertical strings (IC86) arranged in an approximately hexagonal geometry, instrumenting a volume of 1 km^3. Each DOM is made of a downward-pointing 10-inch photomultiplier tube (PMT) [24] to detect Cherenkov photons. The DOM includes readout electronics and a high-voltage power supply [25]. The PMT and its electronics are protected by a spherical glass vessel. The optical properties of the ice have been studied and are used to build a detailed response model of the detector [26]. This model includes depth-dependent scattering and absorption, optical anisotropy and tilt. This analysis uses data from the full array as well as one year of data from before IceCube construction was complete, when it consisted of 79 strings (IC79). Since 2010, IceCube has run stably with an average detector uptime greater than 99% [27].

3 Signal and background predictions

3.1 Signal predictions

The first theoretical calculations for SAνs date back to 1991 [1, 2]. The authors modeled gamma-ray, neutrino, antiproton, neutron, and antineutron fluxes that are initiated by the interactions of cosmic rays with the solar atmosphere. The flux originates from the solar disk as cosmic rays that are mirrored in the solar atmosphere are expected to contribute significantly to the flux [1]. While these early predictions were based on semi-analytical calculations, full numerical simulations of the interactions based on the Monte Carlo method have been performed in Ref. [4]. In more recent publications [7, 8], uncertainties in the predicted neutrino energy spectra from the choice of the primary cosmic-ray flux models, particle interaction models, solar density models, and neutrino oscillation parameters are discussed. Neutrinos generated in the atmosphere of a non-magnetic Sun are propagating through the Sun and their attenuation due to absorption is included. The impact of mirroring of charged particles in solar magnetic flux tubes anchored at the bottom of the photosphere is not considered as it is expected to be sub-dominant at energies above 100 GeV [1]. We will discuss the energy dependent spatial distribution of the solar disk flux in Sec. 5.3.1.

Solar atmospheric neutrino fluxes have been implemented in the simulation framework, WIMPSim [28], which we used for our signal prediction. We obtained neutrino fluxes for all neutrino flavor channels. However, for our analysis we only consider the $\nu_\mu + \bar{\nu}_\mu$ channel to benefit from IceCube's excellent angular resolution O(1°). The impact of additional flavor contributions are discussed as part of our systematic uncertainty studies (see Sec. 4 and 5.3).

In Fig. 1, the $\nu_\mu + \bar{\nu}_\mu$ neutrino flux predictions as well as their uncertainties are shown as the shaded regions. The range of the shaded gray area spans the energy spectra of the results published in [8, 30]. The red region represents the simulation results obtained by running the built-in codes in WIMPSim [7, 28]. Neutrino oscillations are fully taken into account when propagating the neutrinos from the Sun to the Earth and appear as wiggles in the theoretical flux predictions. The oscillations of these high-energy neutrinos, however, cannot be resolved due to the limited energy resolution of IceCube. In Fig. 1 we compare the energy spectra from a set of representative models [7, 8]. For the visualization, we sample the flux predictions with coarse energy bins, that were chosen to reflect IceCube's energy response function. Only the parametrized energy flux from Ref. [4] (IT1996) did not include neutrino oscillations. Ref. [6] has shown that if the primary flavor ratio of SAνs ($\nu_e : \nu_\mu : \nu_\tau$) is $(1 : 2 : 0)$, it would be roughly close to $(1 : 1 : 1)$ at Earth. The flavor ratio of the IT1996 fluxes integrated in the range $(10^{2.0}, 10^{7.0})$ GeV is $(0.92, 2.08, 0)$. For simplicity, IT1996 fluxes for $\nu_\mu + \bar{\nu}_\mu + \nu_e + \bar{\nu}_e$ are divided by a factor of 3 to apply neutrino oscillation effect, shown in Fig. 1 as the black line. Newer reference fluxes [7, 8] already include the effect of the oscillations.

We measure the flux normalization of the SAνs in this analysis. A comparison of signal predictions [4, 7, 8] shows that the SAν spectral shapes are similar enough that we are not expected to be sensitive to individual models. We therefore choose one representative baseline energy spectrum (shown as the blue line in Fig. 1). The baseline energy spectrum is chosen from [7] and uses the Hillas-Gaisser 3-generation model [31] for the primary cosmic-ray spectrum, a combination of the Serenelli [32] and the Stein *et al.* [33] models for the solar density profile, and the normal mass ordering.

Finally, we note that the current leading models neglect solar magnetic field effects. These effects influence cosmic-ray propagation and the cascade development, which in turn influence the neutrino signal. The effect of magnetic fields on cosmic-ray propagation can be

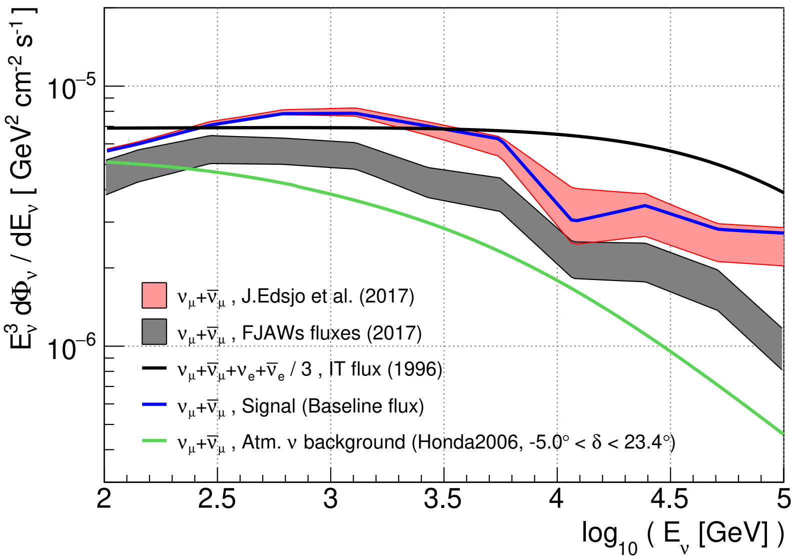

Figure 1. Predicted energy spectra of $\nu_\mu + \bar{\nu}_\mu$ at Earth. The energy spectra are integrated over the solid angle of the solar disk. The fluxes of SAνs are averaged along energy bins to smear out the effects of neutrino oscillation. The blue line is the baseline energy spectrum for systematic studies. The shaded areas cover the range of predictions from each reference (red for [7] and gray for [8]). The black line is the result of [4] divided by a factor of three for neutrino oscillations. The green line is the Honda 2006 flux prediction [29] for terrestrial atmospheric neutrinos, which is time-averaged for the period when the Sun is below the horizon. It is added to demonstrate that the SAν spectrum could be harder than that of neutrinos from the cosmic-ray interactions in the Earth's atmosphere.

indirectly measured through the absorption of cosmic rays in the Sun, which in turn makes a corresponding deficit of cosmic rays in the direction of the Sun. The so-called cosmic-ray Sun shadow has been observed by the Tibet air shower array, including a variation of the intensity correlated with the solar cycle [34]. IceCube also observed the Sun shadow and found a correlation with the sunspot number with a likelihood of 96% [35]. The Sun shadow is sensitive to magnetic field models [36–39] and recent works with numerically computed trajectories of charged cosmic rays confirm the observationally established correlation between the magnitude of the shadowing effect and both the mean sunspot number and the polarity of the magnetic field during a solar cycle [17]. In general, however, high-energy cosmic rays are expected to be energetic enough not to be influenced by magnetic fields. Therefore, only for neutrino production below 200 GeV [1] or 1 TeV [40] is it expected to become significant. Theoretical works using HAWC's Sun shadow observation predict a factor of about two difference in SAν flux between solar minimum and maximum at 200 GeV [40].

3.2 Background predictions and competing signals

Most events in IceCube are downward-going atmospheric muons from cosmic-ray air showers in the Earth atmosphere. These muons can be efficiently rejected by selecting events reconstructed upward, *i.e.* with declination $\delta > -5°$. The well-established event selection for the upward-going neutrino events has achieved a purity of 99.7% [19]. In the remaining sample, the main background arises from terrestrial atmospheric neutrinos produced by decays of mesons within cosmic-rays air showers. Another irreducible, but sub-

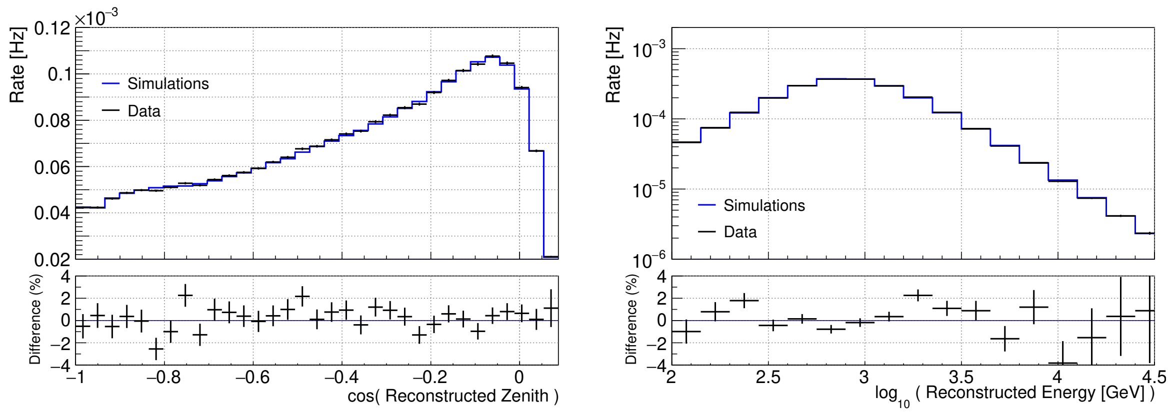

Figure 2. Reconstructed zenith angle and energy distributions for simulations (blue histogram) and data (black crosses, only statistical uncertainties shown). The difference is defined by (Data - Simulations) / Simulations as a percentage. The calculated rates are averaged over the analysis livetime.

dominant background is due to isotropic astrophysical neutrinos. They can be described by an unbroken power-law with a spectral index of 2.19 ± 0.1 and a flux normalization, $\Phi_{100\ \mathrm{TeV}} = 1.01^{+0.26}_{-0.23} \cdot 10^{-18}\mathrm{GeV}^{-1}\mathrm{cm}^{-2}\mathrm{s}^{-1}\mathrm{sr}^{-1}$ at 100 TeV, obtained from fits to the data [19]. The astrophysical neutrinos are included as a background in this analysis, but the uncertainties of the best-fit parameter values are negligible due to it's small contribution to the background rate.

Neutrinos from dark matter annihilations in the Sun could result in a competing signal that has been extensively searched for at neutrino telescopes [41–46]. The expected neutrino spectra from solar dark matter strongly depend on the dark matter mass and annihilation channels. As dark matter annihilations are expected to occur in the center of the Sun, neutrino absorption becomes important for energies above 100 GeV and fluxes are significantly attenuated above that energy. As a result, spectra are expected to be significantly different from that of SAνs [47]. Purely based on event rate expectations at neutrino detectors, one can compute a sensitivity floor for indirect dark matter searches from the Sun [7, 8, 40, 47]. Past dark matter searches were not sensitive enough to have significant backgrounds from solar atmospheric neutrinos. However, in the near future they are expected to reach the neutrino floor from SAνs.

Another competing signal may arise from the interactions of cosmic rays with thermal solar photons. These can interact to form Δ^+ baryons which quickly decay, producing muons and neutrinos from subsequent pion decays [48]. The expected flux from Δ^+ is small and few events are expected in IceCube, so we assume no contributions from the process in this analysis. Larger active volumes, like those proposed for IceCube-Gen2 [49, 50], may be needed to observe events from these interactions.

4 Data sample and simulations

4.1 Data sample

A good angular resolution is necessary to search for SAνs because the angular size of the Sun is $\theta_\odot \sim 0.27°$. Muons traversing the entire detector are reconstructed with good angular resolution as kilometer-long tracks, so-called "through-going muons." We restrict ourselves

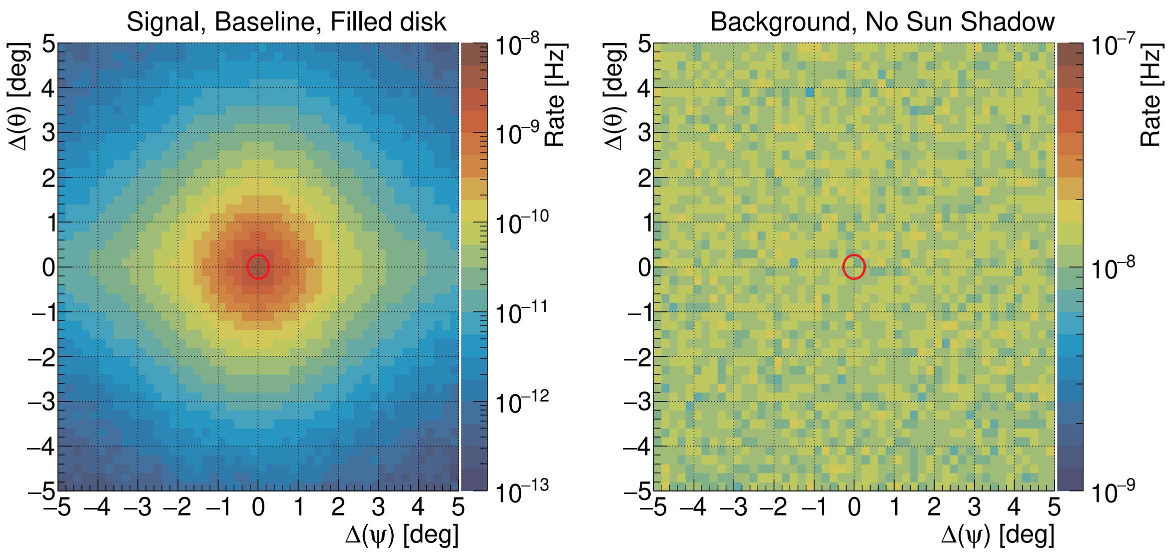

Figure 3. Reconstructed angular distributions from the baseline simulation assuming a *filled disk* (see Sec. 5.3.1). The left and right plots show the expected signal and background, respectively. Axes are differences between the center of the Sun ($\Psi_{\rm Sun}$, $\theta_{\rm Sun}$) and the reconstructed directions (Ψ_ν, θ_ν). The x-axis is the difference in azimuthal angle, Ψ, and the y-axis is the difference in zenith angle, θ, while the z-axis is the event rate averaged for the total analysis livetime. The red circle represents the angular extent of the Sun. Note that the coordinate system does not directly project to the angular separation. The signal from the Sun is not fully symmetric in Θ and Ψ due to the detector geometry and reconstruction uncertainties.

to IceCube's neutrino sample of predominantly through-going muons [21] providing 1.0° and 0.6° median angular resolutions at 1 TeV and 10 TeV neutrino energy, respectively. As the events are not fully contained in the detector volume, the energy resolutions are limited to $\Delta \log_{10}(E/1\text{GeV}) \sim 0.3$ and ~ 0.5 at 1 TeV and 10 TeV, respectively.

The data samples consist of three sub-samples covering a total of seven years. There are three time periods: IC79-2010, IC86-2011, and IC86-(2012-2016). An optimized event selection has been used for each configuration. The ranges of the reconstructed energies are ($10^{2.2}$, $10^{7.2}$) GeV and ($10^{2.0}$, $10^{7.0}$) GeV for IC79-2010 and IC86-(2011,2012-2016). Events below the horizon (declination, $\delta > -5°$) are selected to exclude atmospheric muon events. Unlike Ref. [21], we only consider events where the Sun is below the horizon, resulting in a total analysis livetime of 1406.62 days.

Angular separation ($\theta_\odot$) is defined as an angular distance between the reconstructed position and the center of the Sun at the event trigger time. We use an IceCube internal software implementation that relies on the Positional Astronomy Library (PAL) [51] to obtain the position of the Sun based on the Modified Julian Date and the IceCube detector location. The tracking of the Sun was cross checked with data from NOAA to verify that it agrees within 0.01 degrees. We define a Region of Interest (RoI) as a 5° window around the center of the Sun. The size of the RoI was optimized taking into account the signal sensitivity and the computational time. The sensitivity only marginally improves for larger windows as the RoI contains 96% of the reconstructed signal events.

4.2 Simulations

Simulations are used to obtain probability density functions (PDFs) of the signal and background in the muon neutrino and muon anti-neutrino channels. Simulations samples are taken from the well established and tested IceCube point source analysis [21]. We reuse these simulations but apply selection criteria on the angular separations within the RoI and reweight them with the effective analysis livetime. The background expectations are constructed using simulation, weighted to best-fit parameters for atmospheric and astrophysical neutrino backgrounds found from previous fits to data [19]. In Fig. 2, the comparisons between the simulations for terrestrial atmospheric neutrinos and the total data samples are shown for the reconstructed zenith angle and energy distributions. The simulation samples and the data samples are well-matched within 4% differences.

Signal simulations are obtained by re-weighting the simulated events with the given SAν energy spectrum for muon neutrinos (see Sec. 3.1). The angular separations between the center of the Sun and the events are calculated. The azimuthal directions of the signal events are uniformly scrambled. Events are also randomized in zenith using the probability distribution as a function of angular distance from the center of the Sun for the given source hypothesis. We account for the movement of the Sun in zenith by weighting events using the fraction of livetime spent by the Sun in 30 zenith bins from 85° to 113.4°. In Fig. 3, two-dimensional angular distributions are shown for the baseline signal and background assumptions.

5 Analysis

5.1 Unbinned likelihood analysis

An unbinned likelihood method [52] is applied to find evidence of SAνs in seven years of the data sample. The likelihood function, L_j, for each sub-sample, j, is defined by

$$L_j(n_{s,j}; M_{sig}) = \prod_{i}^{n_{\mathrm{tot},j}} \{\frac{n_{\mathrm{s},j}}{n_{\mathrm{tot},j}} \cdot p_{\mathrm{sig},j}(\theta_i, E_i; M_{\mathrm{sig}}) + (1 - \frac{n_{s,j}}{n_{\mathrm{tot},j}}) \cdot p_{\mathrm{bkg},j}(\theta_i, E_i)\}, \tag{5.1}$$

where j is the index of the sub-sample, i is the event index, $n_{\mathrm{tot},j}$ is the total number of events and $n_{\mathrm{s},j}$ is a number of signal events. For each event, θ_i is the angular separation to the Sun and E_i is the reconstructed muon energy [53]. The function of $p_{\mathrm{sig},j}$ and $p_{\mathrm{bkg},j}$ are the signal and background PDFs evaluated at the location of each event, respectively. In Fig. 4, PDFs of the IC86-(2012-2016) sub-sample are shown. The PDFs are obtained from the simulations and the corresponding likelihood functions are used to study a particular energy spectrum M_{sig}. We combine different sub-samples with a uniform signal emission and use the maximum likelihood estimator to estimate the signal strength. The total likelihood function, L, is a multiplication of the likelihood functions, L_j, for the three sub-samples mentioned in Sec. 4.1. The fractions (f_j) of the total expected signal events for each sub-sample are calculated: $f_j = \bar{n}_{\mathrm{s},j}/\Sigma_k \bar{n}_{\mathrm{s},k}$ where $\bar{n}_{s,j}$ is an expected number of signal events from the simulations. The total likelihood function is redefined as a function of the total signal strength μ with converting $n_{\mathrm{s},j}$ to μf_j:

$$L(\mu) = \prod_{j} \prod_{i}^{n_{\mathrm{tot},j}} \{\frac{\mu f_j}{n_{\mathrm{tot},j}} \cdot p_{\mathrm{sig},j}(\theta_i, E_i|M_{\mathrm{sig}}) + (1 - \frac{\mu f_j}{n_{\mathrm{tot},j}}) \cdot p_{\mathrm{bkg},j}(\theta_i, E_i)\}. \tag{5.2}$$

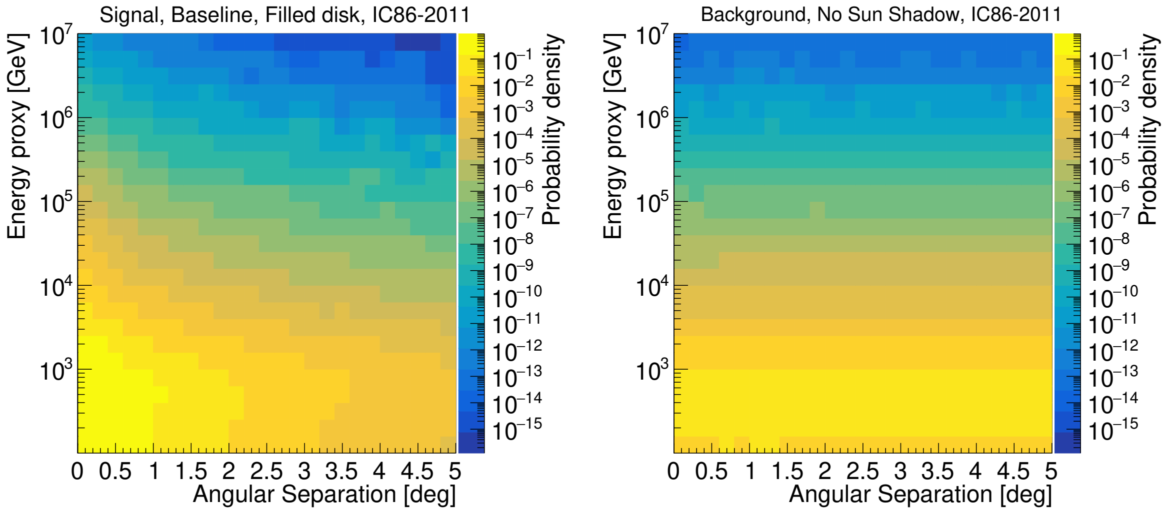

Figure 4. Examples of PDFs in the likelihood functions. The left plot is a signal PDF, while the right plot shows the background PDF for IC86-2011. The probability densities are normalized to 1 in the RoI of the angular separation and energy proxy range. The energy proxy range is all ranges of the reconstructed muon energies in the simulation samples. The binning of the energy proxy is in 0.2 in the log of the reconstructed energy.

The theoretical distribution of flux across the solar disk is expected to depend on neutrino energy via the energy dependence of IceCube reconstructions. To include this correlation, two dimensional PDFs, shown in Fig. 4, are used to model the signal and background distributions in the likelihood functions.

We define the test statistic (TS)

$$\begin{aligned} TS = & \;\; 2\ln L(\hat{\mu})/L(0) \quad \text{for} \quad \hat{\mu} \geq 0 \\ = & -2\ln L(\hat{\mu})/L(0) \quad \text{for} \quad \hat{\mu} < 0, \end{aligned} \tag{5.3}$$

as the likelihood ratio between the best-fit value and the null hypothesis. The range of $\hat{\mu}$ is not restricted to positive values. Therefore, we can track the sign of $\hat{\mu}$ to separately determine sensitivities for a positive or negative signal strength. The negative signs of $\hat{\mu}$ can appear when the alternate hypothesis represents an under-fluctuation relative to the background prediction, especially that the under-fluctuation can be enhanced by the Sun shadow, see Sec. 5.3.3.

5.2 Sensitivity calculations

Pseudo-experiments are conducted to obtain the TS distribution for a given hypothesis. Each pseudo-experiment consists of mock samples generated by random sampling based on each PDF of a certain hypothesis. The number of signal and background events are random variables that are Poisson distributed. The mean of the Poisson distribution for the number of background events is given by the expected number of events from the simulations, $\bar{n}_{\mathrm{bkg}} = 1147.4$ in the RoI. Depending on the hypotheses, the mean for the signal $\bar{\mu}$ is scaled, *e.g.* $\bar{\mu}$=0 for the null hypothesis and $\bar{\mu} = C_s \cdot \bar{n}_{\mathrm{sig}}$, where C_s is a scale factor to test C_s times larger signal hypotheses. $\bar{n}_{\mathrm{sig}}$ is the expected number of signal events determined by combining a given signal model with the simulated detector response. The expected number of background

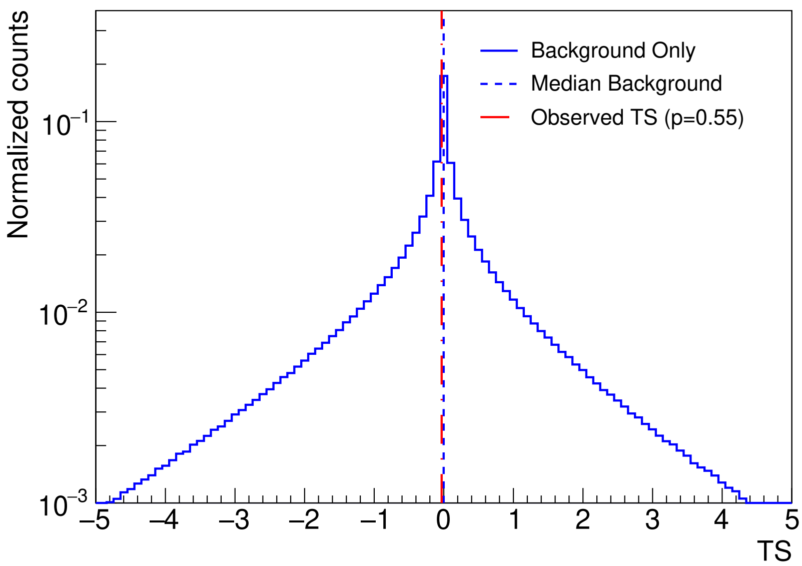

Figure 5. The blue histogram is the *TS* distribution for the background only hypothesis, normalized to 1. The *TS* is negative when the mock sample of the pseudo-experiment contains an under-fluctuation relative to the expected background rate. The blue dashed line is the median of the histogram. The red dashed line is the observed *TS* value from the experimental data.

events, $\bar{n}_{\mathrm{bkg}}$, and signal events, $\bar{n}_{\mathrm{sig}}$, also change with the PDFs according to the hypotheses chosen.

In Fig. 5, the blue histogram is the *TS* distribution for the background-only hypothesis. Negative TS values appear when the likelihood function is maximized with a negative signal strength, due to under-fluctuations in the background rate. The median of the histogram, indicated by the vertical dashed blue line in Fig. 5, is close to zero. The 90% confidence interval (C.I.) is obtained with the Feldman-Cousins method [54] for each alternate hypothesis. μ_{90} is defined by $\bar{\mu}$ of the Poisson mean when the minimum of the 90% C.I. is larger than the median of the *TS* distribution for the null hypothesis. The 90% confidence level (C.L.) upper sensitivities are set with $\mu_{90} = C_{s,90} \cdot \bar{n}_{\mathrm{sig}}$ for each SAν flux model given by Refs. [4, 7, 8]. PDFs are used in the likelihood functions and the random sampling for the mock samples of the pseudo-experiments. The sensitivities to each flux model are calculated with the corresponding PDFs. The sensitivity to the baseline signal spectrum is shown as part of our final result, see the red solid line in Fig. 8. It is 12.8 times larger than the theoretical expectation from the baseline model flux [7].

5.3 Systematic uncertainties

We investigate how the sensitivity of our analysis depends on different choices for flux distributions on the solar disk, oscillation parameters, the effect of the Sun shadow on the backgrounds and detector uncertainties. The differences between the sensitivities are quantified relative to the baseline model as systematic uncertainties.

5.3.1 Flux distribution on the solar disk

High-energy neutrinos above 1 TeV will be strongly suppressed when they propagate through the center of the Sun ($\theta_\odot = 0°$), while the attenuation is much weaker at the edge of the

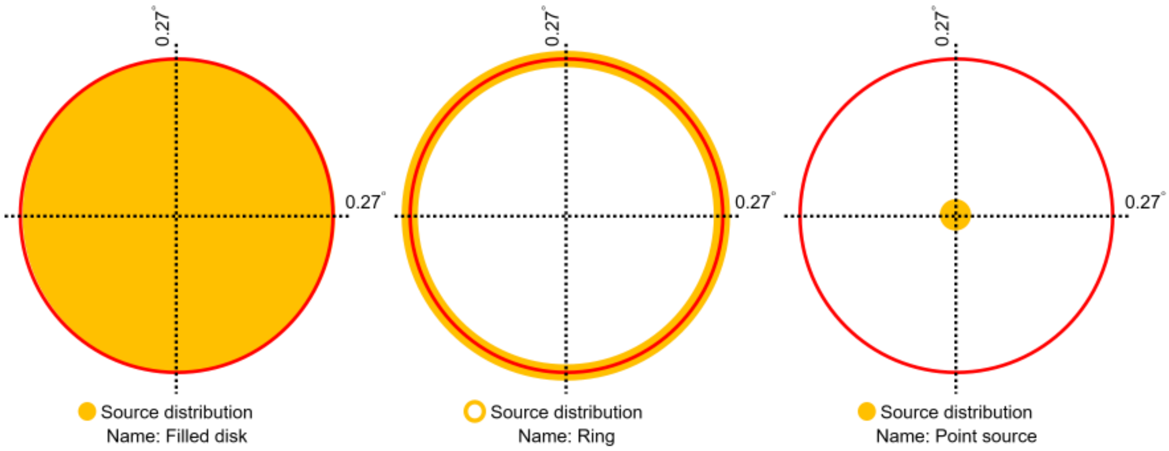

Figure 6. Schematic diagrams for the extreme cases of the distribution of the neutrino flux on the solar disk. The red ring represents the scale of the Sun as $\theta_\odot = 0.266°$. The orange regions represent the distributions of the signal. Left: the signal is uniformly distributed in the solar disk (*Filled disk*, used as baseline). Middle: the signal is emitted at the edge of the Sun (*Ring*). Right: the signal only emanates from the center of the Sun (*Point source*).

Sun ($\theta_\odot \simeq 0.27°$). For instance, the survival probability is larger than $\sim 90\%$ for neutrino energies below 100 TeV [7] at the edge. On the other hand, $\sim 20\%$ ($\sim 35\%$) of 100 GeV neutrinos (anti-neutrinos) survive when they traverse the entire Sun at the center and they are almost completely absorbed above 1 TeV. Therefore, the high-energy events mostly arise from the edge of the Sun. The low-energy signal events emanate relatively uniformly over the solar disk while the high-energy neutrino signal is expected to have a dip in the central region. If we consider magnetic field effects, however, these could act differently due to cosmic-ray mirroring, providing additional contributions in particular toward the center of the disk. This would presumably lead to a more uniform distribution for low energies. As a model-independent method, we consider three extreme cases for the spatial distribution on the disk, shown in Fig. 6. Our baseline model is *Filled Disk* where the signals are uniformly distributed on the solar disk. The simplest assumption is that all neutrinos are coming from the center of the Sun, named *Point Source*. This leads to the best sensitivity with 3% improvement compared to the baseline model. In contrast, *Ring* assumes that the signals are only located at the edge of the Sun. For high-energy neutrinos, the distribution is expected close to *Ring* due to absorption across the solar core. The fluxes are equally normalized for all cases. The true spatial distribution depends on the neutrino energy. We adopt the *Filled Disk* as our baseline and use the two other extreme cases to evaluate the systematic uncertainty due to the choice of the source distribution.

5.3.2 Neutrino oscillation parameters

After SAνs are produced in the Sun, the neutrinos oscillate while propagating to the Earth. The uncertainties on the oscillation parameters can alter the energy spectrum. The oscillation parameters used for the baseline energy spectrum are listed in the column denoted as baseline in Tab. 1. We checked the effect of varying the parameters by 1σ on the energy spectrum. Also, the best-fit values for θ_{23} in the both octants are considered. The uncertainties on

	Baseline	1σ		Octant
$\Delta m^2_{32}/10^{-3}$ (eV^2)	2.51	± 0.05	-2.56 ± 0.04	
$\Delta m^2_{21}/10^{-5}$ (eV^2)	7.53	± 0.18		
$\sin^2\theta_{12}/10^{-1}$	3.07	± 0.13		
$\sin^2\theta_{13}/10^{-2}$	2.12	± 0.08		
$\sin^2\theta_{23}/10^{-1}$	4.17	$+0.25$ -0.28	$4.21 + 0.33$ -0.25	Octant 1
		6.21 5.67	$5.92 + 0.23$ -0.30	Octant 2
Mass Ordering	Normal		Inverted	

Table 1. The neutrino oscillation parameters for the flux calculation in WIMPSim. The values are the best-fit results of Ref. [55]. The second column named "Baseline" lists the parameters for the baseline energy spectrum. The energy spectra for the signal are obtained by WIMPSim, where we independently vary a parameter in 1 σ region and allow $\sin^2\theta_{23}$ to lie in either octants.

neutrino oscillation parameters are treated as systematic uncertainties but the sensitivities for each mass ordering are calculated separately for the energy spectra given by Ref. [7].

5.3.3 Sun shadow effect on the backgrounds

The cosmic-ray flux coming from the direction of the Sun is expected to be less than that from other directions because cosmic rays are absorbed by the Sun itself, creating what is referred to as the Sun shadow. The Sun shadow effect has been observed as a deficit of atmospheric muons [35, 56]. The angular extent of the deficit can be approximated with one-sided Gaussian functions for each season. While we use the case without the Sun shadow as the baseline, the Sun shadow should also reduce the terrestrial atmospheric neutrinos which are the dominant background in this analysis. However, the deficit of the terrestrial atmospheric neutrinos by the Sun shadow has not been studied before. To take this into account, we assume that the neutrino rate decreases with the same fractional strength and angular dependence as the muons studied in Ref. [35]. In simulations, the terrestrial atmospheric neutrino events are re-weighted with the one-sided Gaussian functions of Eq. 5.4:

$$\Delta N_\nu / N_\nu = -A \cdot \exp\left(-\theta_\odot^2 / 2\sigma^2\right) \begin{cases} A = 0.11\,,\ \sigma = 0.53^\circ \text{ for IC79-2010} \\ A = 0.08\,,\ \sigma = 0.49^\circ \text{ for IC86-2011} \\ A = 0.07\,,\ \sigma = 0.57^\circ \text{ for IC86-(2012-2016)}, \end{cases} \tag{5.4}$$

where A and σ are the best-fit parameters for the observed muon deficits by IceCube [35]. The parameters for IC86-(2012-2016) are averaged values to match time period of the sub-sample (see Sec. 4). The parameters are time-dependent because they are correlated with solar activities [17, 35]. Uncertainties on the best-fit parameters A and σ are $\sim 10\%$. Although the deficit of the terrestrial atmospheric neutrinos is expected, we choose to set the baseline background predictions without the Sun shadow effect. Thereby, we have taken a conservative approach in the analysis, which requires a larger signal for a discovery. The Sun shadow effect is included as a systematic uncertainty.

Sources	Systematic Uncertainties	Comments
Detection efficiency of DOM	(-15%, + 11%)	
Absorption and scattering efficiency of ice	(-5%, +12%)	
Photo-nuclear interaction	(-3%, +4%)	Uncertainties for high-energy muons
Morphology	(-3%, +3%)	*Filled disk* $\rightarrow$ *Ring*, *Point source*
Sun shadow	-11%	w/o Sun shadow $\rightarrow$ w/ Sun shadow
ν_τ,$\bar{\nu}_\tau$ contribution	4%	ν_μ,$\bar{\nu}_\mu$ $\rightarrow$ ν_μ,$\bar{\nu}_\mu$,ν_τ,$\bar{\nu}_\tau$
ν oscillation parameters	<1%	
Total	(-19.7%, +17.8%)	Assumes uncorrelated uncertainties

Table 2. Summary of impact on sensitivity. A plus sign corresponds to an improved sensitivity.

5.3.4 Uncertainty calculations

The uncertainties of the sensitivities for the source distributions, neutrino oscillation parameters in the signal prediction and the Sun shadow effect in the background prediction are calculated with the same simulation samples. We randomize the positions of each signal event from the distribution of locations allowed by each Sun model. The same simulations are used for the oscillation parameters and the Sun shadow effect, but the weights in the simulations are modified with the corresponding energy spectra and the deficit rates, respectively. Another main systematic uncertainty arises from standard detector uncertainties including the optical efficiency of DOMs for the Cherenkov light detection [24], the optical absorption and scattering properties of the ice [57], and the uncertainties on photo-nuclear interaction cross sections of high-energy muons [58–64]. The same simulations and detector uncertainties are used as in Ref. [21].

We calculate the sensitivities for the systematic uncertainties as alternate hypotheses. The signal and background PDFs for the baseline are tested against events sampled from PDFs generated from variations of the systematic uncertainties. The uncertainties of the sensitivities are quantified as the differences of the scale factor $C_{s,90}$ when the energy spectrum of the signal is identical to the baseline. The uncertainties of the neutrino oscillation parameters change the shape of the SAν spectra. To quantify the systematic uncertainties, the differences of the μ_{90} are used for the uncertainties of the neutrino oscillation parameters.

Detector uncertainties give the largest systematic uncertainties in this analysis. When we vary the efficiency of DOMs by $\pm10\%$, the sensitivity changes in the range of $(-15, +11)\%$, with positive values indicating improved sensitivity. Simulation data sets with different optical absorption and scattering lengths of the ice are available for the values of $(+10, 0)\%$, $(0, +10)\%$ and $(-7.1, -7.1)\%$. We used those simulations to estimate the uncertainties due to ice properties and they affect the sensitivity by -5% to 12%. The same simulation samples in Ref. [21] are used for studying photo-nuclear interaction models of high energy muons [58–64]. This leads to uncertainties on the sensitivity ranging from -3% to 4%. We consider this estimate to be conservative as the models represent extreme cases which are outdated [21].

The neutrino oscillation parameters introduce less than 1% uncertainty. Tests of the

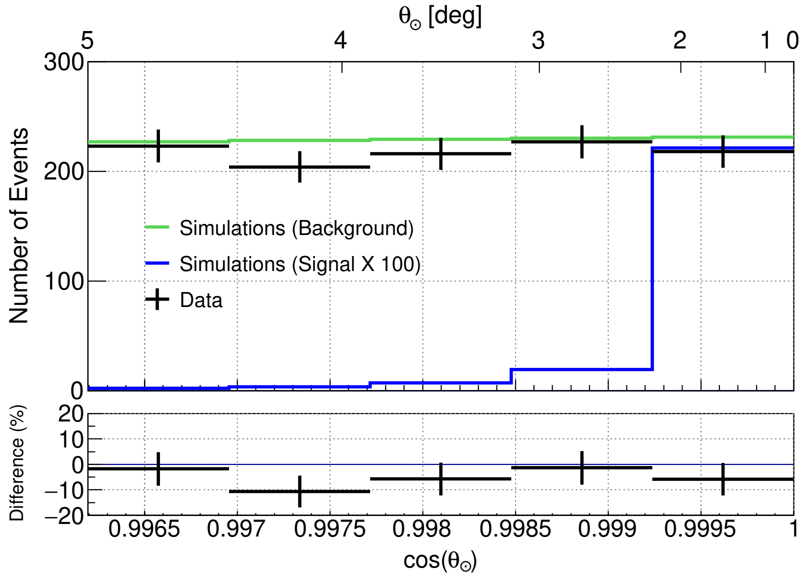

Figure 7. Event distribution in the angular separation ($\theta_{\odot}$) within the RoI. Black crosses represent the experimental data, the green histogram shows the background prediction without the Sun shadow effect. The blue histogram shows the baseline signal prediction scaled by a factor of 100. The simulation and data are shown for the winter season. The difference is defined as (Data - Simulations) / Simulations. This figure is only used for visualization of the data. A binned representation of it is shown here, however, the analysis uses an unbinned likelihood method.

Ring and *Point source* emission distributions yield an uncertainty of $\pm 3\%$. As an uncertainty of the background predictions, the Sun shadow effect has been studied. Compared to the baseline background prediction, the number of background events decreases near the Sun due to the shadow effect. As a result, the likelihood function is maximized with a negative signal strength as the under-fluctuation of the null hypothesis. With the Sun shadow included in the background prediction, a larger $\bar{\mu}$ is necessary to obtain the same sensitivity level with the baseline prediction, hence it increases by 11%.

The simulations assume only muon neutrino and muon anti-neutrino interactions. The fluxes of $\nu_\tau + \bar{\nu}_\tau$ for SAνs can be calculated with WIMPSim for the baseline energy spectrum. Similar amplitudes of $\nu_\tau + \bar{\nu}_\tau$ and $\nu_\mu + \bar{\nu}_\mu$ fluxes are expected through neutrino oscillations from the Sun to the Earth. However, the detection efficiency for $\nu_\tau + \bar{\nu}_\tau$ is much smaller. When we add the additional contribution on the signal by $\nu_\tau + \bar{\nu}_\tau$ using the simulations used in Ref. [21], the sensitivities improves by 4%. The contribution from $\nu_e + \bar{\nu}_e$ is negligible due to the event selection strongly favoring track-like events.

Assuming fully uncorrelated uncertainties, the total uncertainty on the median sensitivity is -19.7% to $+17.8\%$ and is dominated by detector uncertainties. Table 2 summarizes the systematic studies. The systematic uncertainties on sensitivities are shown as the red region as part of the final result in Fig. 8. The systematic uncertainties are similar to those in a previous study with the same samples [21] but the results are slightly distinct because we track the Sun rather than point sources at specific zenith angles.

6 Results

For visualization we show the observed data in the RoI and compare it to the background expectations in a binned representation, however, the analysis uses an unbinned likelihood method. In the top panel of Fig. 7, the angular distribution of the experimental data in the RoI is shown by the black crosses. The observed data are within 10% of the background prediction (green histogram), and the number of events in the RoI is statistically compatible with the background expectation at 1.75σ. The best-fit values $\hat{\mu}$ for all energy spectra are shown in Tab. 3 and are always negative, indicating an under-fluctuation in the data relative to the expected background. No evidence of SAνs is found in seven years of IceCube data. The observed TS for the baseline signal prediction is the red dashed line in Fig. 5. It is very close to the median of the TS distribution for the null hypothesis, with an observed p-value of 0.55. Here, the p-value is defined as the area of the TS distribution above the observed TS value.

The observed p-value being larger than 0.5 indicates that there is a slight under--fluctuation in the background expectation. We place a 90% C.L. upper limit for μ_{90}, when the lower edge of the 90% C.I. is larger than the observed TS value. In Fig. 8, the black dashed line represents this limit. The values obtained for μ_{90} ($C_{s,90}$) are 36.5 (13.0). At 1 TeV, the limit on the flux normalization is $1.02^{+0.20}_{-0.18} \cdot 10^{-13}$ GeV^{-1}cm^{-2}s^{-1} including the systematic uncertainties. Table 3 contains the full analysis results with limits on all SAν flux models. The limits calculated on the basis of Ref. [7] and Ref. [8] turn out to rather similar. The strictest limit is obtained for the parametrized energy spectrum of Ref. [4] as it predicts the hardest spectrum at high energy (see Fig. 1).

7 Conclusion and discussion

We have performed the first experimental search for SAν using data collected by the IceCube Neutrino Observatory during a 7 year period for the austral winter season when the declination of the Sun is above -5°. An unbinned likelihood analysis was performed with a total analysis livetime of 1406.62 days but no evidence for SAνs was found in the experimental data. The experimental data show an under-fluctuation relative to the background prediction and are consistent with a statistical fluctuation in the data. After inclusion of systematic uncertainties on the background prediction and signal efficiency, a 90% confidence level upper limit is placed on the SAν flux at 1 TeV of $1.02^{+0.20}_{-0.18} \cdot 10^{-13}$ GeV^{-1}cm^{-2}s^{-1} for the benchmark signal energy spectrum from Ref. [7]. At present, our limit is about a factor of 13 larger than the baseline signal expectation. The results presented in this paper do not allow us to distinguish between various model predictions. In the future several improvements can be expected that will result in a better sensitivity to solar atmospheric neutrinos. The IceCube Upgrade will increase the acceptance of neutrinos down to a few GeV and a comprehensive calibration campaign is expected to reduce uncertainties related to ice properties, which will reduce reconstruction uncertainties in energy and arrival direction. Next-generation neutrino observatories, such as IceCube-Gen2 [50] or KM3NeT [66], will significantly increase acceptance of multi-TeV events, which are expected to have low atmospheric neutrino backgrounds. They could provide sufficient sensitivity to find evidence of SAνs.

The SAν production mechanism is closely related to that of gamma rays from the solar disk. Based on public Fermi data it has been shown that the gamma-ray flux from the solar disk is about one order of magnitude higher than predicted [1] and that the flux shows

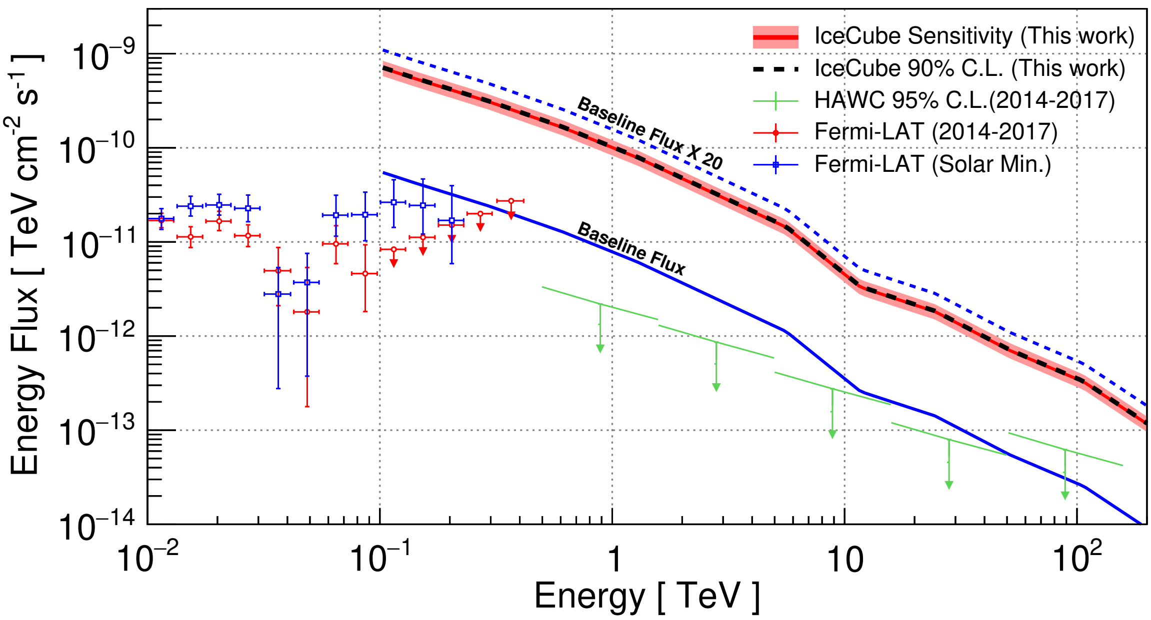

Figure 8. IceCube 90% C.L. upper limit is the black dashed line assumed the signal following the baseline flux expectation, the blue solid line. For comparison, the blue dotted line shows the baseline flux scaled by a factor of 20. The red shaded band illustrates the corresponding uncertainty of the baseline model. In addition, we include results from gamma-ray observations in the plot. Red and blue crosses are the observations of Fermi-LAT [13, 15]; green points correspond to HAWC's 95% C.L limit [16, 65].

a significant time variation that anti-correlates with solar activity [12, 13, 15]. We point out that our IceCube dataset, which consists of all available data at the time of the analysis, covers the period from May 2010 till May 2017 and hence does not include the solar minimum. Similar to the observed flux increase in gamma rays, the SAν flux is expected to be enhanced during the solar minimum [40]. Based on the current data and models predictions, we point out that there is a considerable uncertainty in the flux expectations of solar gamma-rays and neutrinos. In addition, energetic gamma-ray events are observed primarily during the solar minimum. A continuation of this analysis during the solar minimum of 2019-2020 is in progress.

An observation of solar atmospheric neutrinos would be important to understand solar atmospheric magnetic fields, cosmic ray interactions in the solar atmosphere, and cosmic ray propagation in the inner solar system. Furthermore, a measurement of the SAν flux is also essential for solar dark matter searches to characterize the SAν sensitivity floor [7, 8, 47]. If the SAν flux is experimentally measured, it will provide the normalization of this irreducible background for solar dark matter searches.

Given the expected sensitivity of this analysis we decided to only test one signal hypothesis, namely our baseline model. In future analyses with improved sensitivity, differential flux limits could be produced and a more model independent approach could be taken to probe different energy ranges.

Lastly, an observation of the SAνs can be exploited as a calibration source for neutrino telescopes in the future. An observation of a high-energy neutrino signal from the Sun would only be the second of its kind, following the recent evidence of a high-energy neutrino signal from the blazar TXS 0506+056 [67, 68].

Acknowledgments

The IceCube collaboration acknowledges the significant contributions to this manuscript from Seongjin In and Carsten Rott. The authors gratefully acknowledge the support from the following agencies and institutions: USA – U.S. National Science Foundation-Office of Polar Programs, U.S. National Science Foundation-Physics Division, Wisconsin Alumni Research Foundation, Center for High Throughput Computing (CHTC) at the University of Wisconsin-Madison, Open Science Grid (OSG), Extreme Science and Engineering Discovery Environment (XSEDE), U.S. Department of Energy-National Energy Research Scientific Computing Center, Particle astrophysics research computing center at the University of Maryland, Institute for Cyber-Enabled Research at Michigan State University, and Astroparticle physics computational facility at Marquette University; Belgium – Funds for Scientific Research (FRS-FNRS and FWO), FWO Odysseus and Big Science programmes, and Belgian Federal Science Policy Office (Belspo); Germany – Bundesministerium für Bildung und Forschung (BMBF), Deutsche Forschungsgemeinschaft (DFG), Helmholtz Alliance for Astroparticle Physics (HAP), Initiative and Networking Fund of the Helmholtz Association, Deutsches Elektronen Synchrotron (DESY), and High Performance Computing cluster of the RWTH Aachen; Sweden – Swedish Research Council, Swedish Polar Research Secretariat, Swedish National Infrastructure for Computing (SNIC), and Knut and Alice Wallenberg Foundation; Australia – Australian Research Council; Canada – Natural Sciences and Engineering Research Council of Canada, Calcul Québec, Compute Ontario, Canada Foundation for Innovation, WestGrid, and Compute Canada; Denmark – Villum Fonden, Danish National Research Foundation (DNRF), Carlsberg Foundation; New Zealand – Marsden Fund; Japan – Japan Society for Promotion of Science (JSPS) and Institute for Global Prominent Research (IGPR) of Chiba University; Korea – National Research Foundation of Korea (NRF); Switzerland – Swiss National Science Foundation (SNSF); United Kingdom – Department of Physics, University of Oxford.

References

[1] D. Seckel, T. Stanev, and T. K. Gaisser, *Signatures of cosmic-ray interactions on the solar surface*, *Astrophys. J.* **382** (1991) 652–666.

[2] I. V. Moskalenko, S. Karakula, and W. Tkaczyk, *The Sun as the source of VHE neutrinos*, *Astron. Astrophys.* **248** (1991) L5–L6.

[3] I. V. Moskalenko and S. Karakula, *Very high-energy neutrinos from the sun*, *J. Phys.* **G19** (1993) 1399–1406.

[4] G. Ingelman and M. Thunman, *High-energy neutrino production by cosmic ray interactions in the sun*, *Phys. Rev.* **D54** (1996) 4385–4392, [hep-ph/9604288].

[5] C. Hettlage, K. Mannheim, and J. G. Learned, *The Sun as a high-energy neutrino source*, *Astropart. Phys.* **13** (2000) 45–50, [astro-ph/9910208].

[6] G. L. Fogli, E. Lisi, A. Mirizzi, D. Montanino, and P. D. Serpico, *Oscillations of solar atmosphere neutrinos*, *Phys. Rev.* **D74** (2006) 093004, [hep-ph/0608321].

[7] J. Edsjö, J. Elevant, R. Enberg, and C. Niblaeus, *Neutrinos from cosmic ray interactions in the Sun*, *JCAP* **1706** (2017), no. 06 033, [arXiv:1704.0289].

[8] C. A. Argüelles, G. de Wasseige, A. Fedynitch, and B. J. P. Jones, *Solar Atmospheric Neutrinos and the Sensitivity Floor for Solar Dark Matter Annihilation Searches*, *JCAP* **1707** (2017), no. 07 024, [arXiv:1703.0779].

[9] A. Fedynitch, J. Becker Tjus, and P. Desiati, *Influence of hadronic interaction models and the cosmic ray spectrum on the high energy atmospheric muon and neutrino flux*, *Phys. Rev.* **D86** (2012) 114024, [arXiv:1206.6710].

[10] E. Orlando and A. W. Strong, *Gamma-ray emission from the solar halo and disk: a study with EGRET data*, *Astron. Astrophys.* **480** (2008) 847, [arXiv:0801.2178].

[11] **Fermi-LAT** Collaboration, A. A. Abdo *et. al.*, *Fermi-LAT Observations of Two Gamma-Ray Emission Components from the Quiescent Sun*, *Astrophys. J.* **734** (2011) 116, [arXiv:1104.2093].

[12] K. C. Y. Ng, J. F. Beacom, A. H. G. Peter, and C. Rott, *First Observation of Time Variation in the Solar-Disk Gamma-Ray Flux with Fermi*, *Phys. Rev.* **D94** (2016), no. 2 023004, [arXiv:1508.0627].

[13] T. Linden, B. Zhou, J. F. Beacom, A. H. G. Peter, K. C. Y. Ng, and Q.-W. Tang, *Evidence for a New Component of High-Energy Solar Gamma-Ray Production*, *Phys. Rev. Lett.* **121** (2018), no. 13 131103, [arXiv:1803.0543].

[14] M. N. Mazziotta, P. De La Torre Luque, L. Di Venere, A. Fassò, A. Ferrari, F. Loparco, P. R. Sala, and D. Serini, *Cosmic-ray interactions with the Sun using the FLUKA code*, *Phys. Rev.* **D101** (2020), no. 8 083011, [arXiv:2001.0993].

[15] Q.-W. Tang, K. C. Y. Ng, T. Linden, B. Zhou, J. F. Beacom, and A. H. G. Peter, *Unexpected dip in the solar gamma-ray spectrum*, *Phys. Rev.* **D98** (2018), no. 6 063019, [arXiv:1804.0684].

[16] **HAWC** Collaboration, A. Albert *et. al.*, *First HAWC Observations of the Sun Constrain Steady TeV Gamma-Ray Emission*, *Phys. Rev.* **D98** (2018), no. 12 123011, [arXiv:1808.0562].

[17] J. Becker Tjus, P. Desiati, N. Döpper, H. Fichtner, J. Kleimann, M. Kroll, and F. Tenholt, *Cosmic-Ray Propagation Around the Sun - Investigating the Influence of the Solar Magnetic Field on the Cosmic-Ray Sun Shadow*, *Astron. Astrophys.* **633** (2020) A83, [arXiv:1903.1263].

[18] **IceCube** Collaboration, M. G. Aartsen *et. al.*, *Observation and Characterization of a Cosmic Muon Neutrino Flux from the Northern Hemisphere using six years of IceCube data*, *Astrophys. J.* **833** (2016), no. 1 3, [arXiv:1607.0800].

[19] **IceCube** Collaboration, C. Haack and C. Wiebusch, *A measurement of the diffuse astrophysical muon neutrino flux using eight years of IceCube data.*, *PoS* **ICRC2017** (2018) 1005.

[20] **IceCube** Collaboration, M. G. Aartsen *et. al.*, *Evidence for Astrophysical Muon Neutrinos from the Northern Sky with IceCube*, *Phys. Rev. Lett.* **115** (2015), no. 8 081102, [arXiv:1507.0400].

[21] **IceCube** Collaboration, M. G. Aartsen *et. al.*, *Search for steady point-like sources in the astrophysical muon neutrino flux with 8 years of IceCube data*, *Eur. Phys. J.* **C79** (2019), no. 3 234, [arXiv:1811.0797].

[22] **IceCube** Collaboration, R. Abbasi *et. al.*, *IceTop: The surface component of IceCube*, *Nucl. Instrum. Meth.* **A700** (2013) 188–220, [arXiv:1207.6326].

[23] **IceCube** Collaboration, A. Achterberg *et. al.*, *First Year Performance of The IceCube Neutrino Telescope*, *Astropart. Phys.* **26** (2006) 155–173, [astro-ph/0604450].

[24] **IceCube** Collaboration, R. Abbasi *et. al.*, *Calibration and Characterization of the IceCube Photomultiplier Tube*, *Nucl. Instrum. Meth.* **A618** (2010) 139–152, [arXiv:1002.2442].

[25] **IceCube** Collaboration, R. Abbasi *et. al.*, *The IceCube Data Acquisition System: Signal Capture, Digitization, and Timestamping*, *Nucl. Instrum. Meth.* **A601** (2009) 294–316, [arXiv:0810.4930].

[26] **IceCube** Collaboration, M. G. Aartsen *et. al.*, *Measurement of South Pole ice transparency with the IceCube LED calibration system*, *Nucl. Instrum. Meth.* **A711** (2013) 73–89, [arXiv:1301.5361].

[27] **IceCube** Collaboration, M. G. Aartsen *et. al.*, *The IceCube Neutrino Observatory: Instrumentation and Online Systems*, *JINST* **12** (2017), no. 03 P03012, [arXiv:1612.0509].

[28] J. Edsjö, J. Elevant, and C. Niblaeus, "WimpSim Neutrino Monte Carlo." http://wimpsim.astroparticle.se/, last accessed on 11/25/19.

[29] M. Honda, T. Kajita, K. Kasahara, S. Midorikawa, and T. Sanuki, *Calculation of atmospheric neutrino flux using the interaction model calibrated with atmospheric muon data*, *Phys. Rev.* **D75** (2007) 043006, [astro-ph/0611418].

[30] C. A. Argüelles, G. de Wasseige, A. Fedynitch, and B. J. P. Jones, "FJAWs solar atmopsheric neutrino fluxes." http://www-hep.uta.edu/~bjones/FJAWs/index.html, last accessed on 11/25/19.

[31] T. K. Gaisser, *Spectrum of cosmic-ray nucleons, kaon production, and the atmospheric muon charge ratio*, *Astropart. Phys.* **35** (2012) 801–806, [arXiv:1111.6675].

[32] A. Serenelli, S. Basu, J. W. Ferguson, and M. Asplund, *New Solar Composition: The Problem With Solar Models Revisited*, *Astrophys. J.* **705** (2009) L123–L127, [arXiv:0909.2668].

[33] R. F. Stein and Å. Nordlund, *Simulations of Solar Granulation. I. General Properties*, *Astrophys. J.* **499** (May, 1998) 914–933.

[34] **Tibet AS-gamma** Collaboration, M. Amenomori *et. al.*, *Probe of the Solar Magnetic Field Using the Cosmic-Ray Shadow of the Sun*, *Phys. Rev. Lett.* **111** (2013), no. 1 011101, [arXiv:1306.3009].

[35] **IceCube** Collaboration, M. G. Aartsen *et. al.*, *Detection of the Temporal Variation of the Sun's Cosmic Ray Shadow with the IceCube Detector*, *Astrophys. J.* **872** (2019), no. 2 133, [arXiv:1811.0201].

[36] K. H. Schatten, J. M. Wilcox, and N. F. Ness, *A model of interplanetary and coronal magnetic fields*, *Sol. Phys.* **6** (Mar., 1969) 442–455.

[37] K. Hakamada, *A simple method to compute spherical harmonic coefficients for the potential model of the coronal magnetic field*, *Solar Physics* **159** (Jun, 1995) 89–96.

[38] T. J. Bogdan and B. C. Low, *The three-dimensional structure of magnetostatic atmospheres. II - Modeling the large-scale corona*, *The Astrophysical Journal* **306** (July, 1986) 271–283.

[39] X. Zhao and J. T. Hoeksema, *Prediction of the interplanetary magnetic field strength*, *Journal of Geophysical Research: Space Physics* **100** (1995), no. A1 19–33.

[40] M. Masip, *High energy neutrinos from the Sun*, *Astropart. Phys.* **97** (2018) 63–68, [arXiv:1706.0129].

[41] M. Danninger and C. Rott, *Solar WIMPs unravelled: Experiments, astrophysical uncertainties, and interactive tools*, *Phys. Dark Univ.* **5-6** (2014) 35–44, [arXiv:1509.0823].

[42] **IceCube** Collaboration, M. G. Aartsen *et. al.*, *Search for dark matter annihilations in the Sun with the 79-string IceCube detector*, *Phys. Rev. Lett.* **110** (2013), no. 13 131302, [arXiv:1212.4097].

[43] **IceCube** Collaboration, M. G. Aartsen *et. al.*, *Search for annihilating dark matter in the Sun with 3 years of IceCube data*, *Eur. Phys. J.* **C77** (2017), no. 3 146, [arXiv:1612.0594]. [Erratum: Eur. Phys. J.C79,no.3,214(2019)].

[44] **Super-Kamiokande** Collaboration, K. Choi *et. al.*, *Search for neutrinos from annihilation of captured low-mass dark matter particles in the Sun by Super-Kamiokande*, *Phys. Rev. Lett.* **114** (2015), no. 14 141301, [arXiv:1503.0485].

[45] **ANTARES** Collaboration, S. Adrian-Martinez *et. al.*, *Limits on Dark Matter Annihilation in the Sun using the ANTARES Neutrino Telescope*, *Phys. Lett.* **B759** (2016) 69–74, [arXiv:1603.0222].

[46] **IceCube** Collaboration, S. In and K. Wiebe, *Latest results and sensitivities for solar dark matter searches with IceCube*, *PoS* **ICRC2017** (2018) 912.

[47] K. C. Y. Ng, J. F. Beacom, A. H. G. Peter, and C. Rott, *Solar Atmospheric Neutrinos: A New Neutrino Floor for Dark Matter Searches*, *Phys. Rev.* **D96** (2017), no. 10 103006, [arXiv:1703.1028].

[48] K. K. Andersen and S. R. Klein, *High energy cosmic-ray interactions with particles from the Sun*, *Phys. Rev.* **D83** (2011) 103519, [arXiv:1103.5090].

[49] **IceCube** Collaboration, M. G. Aartsen *et. al.*, *IceCube-Gen2: A Vision for the Future of Neutrino Astronomy in Antarctica*, arXiv:1412.5106.

[50] **IceCube-Gen2** Collaboration, M. Aartsen *et. al.*, *IceCube-Gen2: The Window to the Extreme Universe*, arXiv:2008.0432.

[51] T. Jenness and D. S. Berry, *PAL: A Positional Astronomy Library*, in *Astronomical Data Analysis Software and Systems XXII* (D. N. Friedel, ed.), vol. 475 of *Astronomical Society of the Pacific Conference Series*, p. 307, Oct., 2013.

[52] J. Braun, J. Dumm, F. De Palma, C. Finley, A. Karle, and T. Montaruli, *Methods for point source analysis in high energy neutrino telescopes*, *Astropart. Phys.* **29** (2008) 299–305, [arXiv:0801.1604].

[53] **IceCube** Collaboration, R. Abbasi *et. al.*, *An improved method for measuring muon energy using the truncated mean of dE/dx*, *Nucl. Instrum. Meth. A* **703** (2013) 190–198, [arXiv:1208.3430].

[54] G. J. Feldman and R. D. Cousins, *A Unified approach to the classical statistical analysis of small signals*, *Phys. Rev.* **D57** (1998) 3873–3889, [physics/9711021].

[55] **Particle Data Group** Collaboration, M. Tanabashi *et. al.*, *Review of Particle Physics*, *Phys. Rev.* **D98** (2018), no. 3 030001.

[56] **IceCube** Collaboration, M. Aartsen *et. al.*, *Measurements of the Time-Dependent Cosmic-Ray Sun Shadow with Seven Years of IceCube Data – Comparison with the Solar Cycle and Magnetic Field Models*, arXiv:2006.1629.

[57] **IceCube** Collaboration, M. G. Aartsen *et. al.*, *Energy Reconstruction Methods in the IceCube Neutrino Telescope*, *JINST* **9** (2014) P03009, [arXiv:1311.4767].

[58] L. B. Bezrukov and E. V. Bugaev, *Nucleon Shadowing Effects in Photon Nucleus Interaction. (In Russian)*, *Yad. Fiz.* **33** (1981) 1195–1207. [Sov. J. Nucl. Phys.33,635(1981)].

[59] E. V. Bugaev and Yu. V. Shlepin, *Photonuclear interactions of super-high energy muons and tau-leptons*, *Nucl. Phys. Proc. Suppl.* **122** (2003) 341–344.

[60] E. V. Bugaev and Yu. V. Shlepin, *Photonuclear interaction of high-energy muons and tau leptons*, *Phys. Rev.* **D67** (2003) 034027, [hep-ph/0203096].

[61] E. Bugaev, T. Montaruli, Y. Shlepin, and I. A. Sokalski, *Propagation of tau neutrinos and tau leptons through the earth and their detection in underwater / ice neutrino telescopes*, *Astropart. Phys.* **21** (2004) 491–509, [hep-ph/0312295].

[62] H. Abramowicz, E. M. Levin, A. Levy, and U. Maor, *A Parametrization of $\sigma_T(\gamma^* p)$ above the resonance region Q^2 >= 0*, *Phys. Lett.* **B269** (1991) 465–476.

[63] H. Abramowicz and A. Levy, *The ALLM parameterization of σ(tot)(γ* p): An Update*, hep-ph/9712415.

[64] J. H. Koehne, K. Frantzen, M. Schmitz, T. Fuchs, W. Rhode, D. Chirkin, and J. Becker Tjus, *PROPOSAL: A tool for propagation of charged leptons*, *Comput. Phys. Commun.* **184** (2013) 2070–2090.

[65] B. Zhou, K. C. Y. Ng, J. F. Beacom, and A. H. G. Peter, *TeV Solar Gamma Rays From Cosmic-Ray Interactions*, *Phys. Rev.* **D96** (2017), no. 2 023015, [arXiv:1612.0242].

[66] **KM3Net** Collaboration, S. Adrian-Martinez *et. al.*, *Letter of intent for KM3NeT 2.0*, *J. Phys. G* **43** (2016), no. 8 084001, [arXiv:1601.0745].

[67] **IceCube** Collaboration, M. G. Aartsen *et. al.*, *Neutrino emission from the direction of the blazar TXS 0506+056 prior to the IceCube-170922A alert*, *Science* **361** (2018), no. 6398 147–151, [arXiv:1807.0879].

[68] **IceCube, Fermi-LAT, MAGIC, AGILE, ASAS-SN, HAWC, H.E.S.S., INTEGRAL, Kanata, Kiso, Kapteyn, Liverpool Telescope, Subaru, Swift NuSTAR, VERITAS, VLA/17B-403** Collaboration, M. G. Aartsen *et. al.*, *Multimessenger observations of a flaring blazar coincident with high-energy neutrino IceCube-170922A*, *Science* **361** (2018), no. 6398 eaat1378, [arXiv:1807.0881].

[69] N. Grevesse and A. J. Sauval, *Standard Solar Composition*, *Space Sci. Rev.* **85** (1998) 161–174.

[70] T. K. Gaisser, T. Stanev, and S. Tilav, *Cosmic Ray Energy Spectrum from Measurements of Air Showers*, *Front. Phys.(Beijing)* **8** (2013) 748–758, [arXiv:1303.3565].

[71] F. Riehn, R. Engel, A. Fedynitch, T. K. Gaisser, and T. Stanev, *Charm production in SIBYLL*, *EPJ Web Conf.* **99** (2015) 12001, [arXiv:1502.0635].

[72] F. Riehn, R. Engel, A. Fedynitch, T. K. Gaisser, and T. Stanev, *A new version of the event generator Sibyll*, *PoS* **ICRC2015** (2016) 558, [arXiv:1510.0056].

[73] T. K. Gaisser and M. Honda, *Flux of atmospheric neutrinos*, *Ann. Rev. Nucl. Part. Sci.* **52** (2002) 153–199, [hep-ph/0203272].

[74] J. R. Hoerandel, *On the knee in the energy spectrum of cosmic rays*, *Astropart. Phys.* **19** (2003) 193–220, [astro-ph/0210453].

[75] P. Gondolo, G. Ingelman, and M. Thunman, *Charm production and high-energy atmospheric muon and neutrino fluxes*, *Astropart. Phys.* **5** (1996) 309–332, [hep-ph/9505417].

[76] V. I. Zatsepin and N. V. Sokolskaya, *Three component model of cosmic ray spectra from 100-GeV up to 100-PeV*, *Astron. Astrophys.* **458** (2006) 1–5, [astro-ph/0601475].

[77] A. D. Martin, M. G. Ryskin, and A. M. Stasto, *Prompt neutrinos from atmospheric $c\bar{c}$ and $b\bar{b}$ production and the gluon at very small x*, *Acta Phys. Polon.* **B34** (2003) 3273–3304, [hep-ph/0302140].

Energy spectrum (RoI, 1406.62 days)	$\bar{n}_{\mathrm{sig}}$	μ_{90}	$\hat{\mu}$ (Data)	TS (Data)	p-value	$\Phi_{90\%}(1\ \mathrm{TeV})\ [\mathrm{GeV}^{-1}\mathrm{cm}^{-2}\mathrm{s}^{-1}]$
Baseline model: Ingelman & Thunman (1996) [4]						
IT Flux (1996)	2.83	35.09	-2.28	-0.05	0.56	$8.57 \cdot 10^{-14}$
Reference model 1: Edsjö et al. (2017) [7]						
Serenelli [32]-GS98 [69]-H3a [31]-Normal	2.85	36.56	-1.95	-0.03	0.55	$1.01 \cdot 10^{-13}$
Serenelli-Stein [33]-H3a-Normal (Baseline)	2.80	36.52	-1.96	-0.03	0.55	$1.02 \cdot 10^{-13}$
Serenelli-GS98 [69]-H3a-Inverted	2.95	36.26	-1.93	-0.03	0.55	$9.65 \cdot 10^{-14}$
Serenelli-Stein-H3a-Inverted	2.89	36.39	-1.96	-0.03	0.55	$9.89 \cdot 10^{-14}$
Serenelli-GS98-4Gen [70]-Normal	2.70	37.21	-1.93	-0.03	0.55	$1.08 \cdot 10^{-13}$
Serenelli-Stein-4Gen-Normal	2.65	37.30	-2.00	-0.03	0.55	$1.10 \cdot 10^{-13}$
Serenelli-GS98-4Gen-Inverted	2.79	36.98	-1.96	-0.03	0.55	$1.04 \cdot 10^{-13}$
Serenelli-Stein-4Gen-Inverted	2.73	37.06	-1.95	-0.03	0.55	$1.06 \cdot 10^{-13}$
Reference model 2: FJAWs (2017) [8]						
SIBYLL2.3-pp [71, 72]-CombinedGH-H4a [9]	2.16	38.40	-2.08	-0.03	0.56	$1.37 \cdot 10^{-13}$
SIBYLL2.3-pp-GaisserHonda [73]	1.82	38.40	-2.34	-0.04	0.56	$1.66 \cdot 10^{-13}$
SIBYLL2.3-pp-HillasGaisser-H4a [31]	2.17	37.51	-2.07	-0.03	0.56	$1.36 \cdot 10^{-13}$
SIBYLL2.3-pp-PolyGonato [74]	1.74	38.32	-2.19	-0.03	0.56	$1.73 \cdot 10^{-13}$
SIBYLL2.3-pp-Thunman [75]	1.95	38.33	-2.28	-0.04	0.56	$1.55 \cdot 10^{-13}$
SIBYLL2.3-pp-ZatsepinSokolskaya [76]	1.71	37.45	-2.18	-0.04	0.56	$1.72 \cdot 10^{-13}$
SIBYLL2.3-ppMRS [77]-CombinedGH-H4a	2.17	37.53	-2.09	-0.03	0.56	$1.36 \cdot 10^{-13}$
SIBYLL2.3-ppMRS-GaisserHonda	1.82	38.39	-2.34	-0.04	0.56	$1.65 \cdot 10^{-13}$
SIBYLL2.3-ppMRS-HillasGaisser-H4a	2.17	37.44	-2.08	-0.03	0.56	$1.35 \cdot 10^{-13}$
SIBYLL2.3-ppMRS-PolyGonato	1.75	38.22	-2.22	-0.04	0.56	$1.72 \cdot 10^{-13}$
SIBYLL2.3-ppMRS-Thunman	1.95	38.24	-2.29	-0.04	0.56	$1.54 \cdot 10^{-13}$
SIBYLL2.3-ppMRS-ZatsepinSokolskaya	1.71	37.50	-2.21	-0.04	0.56	$1.72 \cdot 10^{-13}$

Table 3. Summary table of the analysis results for corresponding models of the energy spectra from each reference in the first column. "Normal" and "Inverted" in the rows of Ref. [7] refer to the neutrino mass ordering. Columns 2-7 represent the expected number of signal events, $\bar{n}_{\mathrm{sig}}$, the Poisson mean for the 90% C.L. limit, μ_{90}, the maximum likelihood estimator, $\hat{\mu}$, the observed TS value, p-value and the flux limit at 1 TeV, $\Phi_{90\%}(1\ \mathrm{TeV})$.